Micromolar and submicromolar Ca^{2+} spikes regulating distinct cellular functions in pancreatic acinar cells

Koichi Ito, Yasushi Miyashita and Haruo Kasai[1]

Department of Physiology, Faculty of Medicine, University of Tokyo, Hongo, Bunkyo-ku, Tokyo 113, Japan

[1]Corresponding author

Agonists induce Ca^{2+} spikes, waves and oscillations initiating at a trigger zone in exocrine acinar cells via Ca^{2+} release from intracellular Ca^{2+} stores. Using a low affinity ratiometric Ca^{2+} indicator dye, benzothiazole coumarin (BTC), we found that high concentrations of agonists transiently increased Ca^{2+} concentrations to the micromolar range (>10 μM) in the trigger zone. Comparison with results obtained with a high affinity Ca^{2+} indicator dye, fura-2, indicated that fura-2 was in fact saturated with Ca^{2+} during the agonist-induced Ca^{2+} spikes in the trigger zone. We further revealed that the micromolar Ca^{2+} spikes were necessary for inducing exocytosis of zymogen granules investigated using capacitance measurements. In contrast, submicromolar Ca^{2+} spikes selectively gave rise to sequential activation of luminal and basal ion channels. These results suggest new functional diversity in Ca^{2+} spikes and a critical role for the micromolar Ca^{2+} spikes in exocytotic secretion from exocrine acinar cells. Our data also emphasize the value of investigating the Ca^{2+} signalling using low affinity Ca^{2+} indicators.
Keywords: Ca^{2+} gradients/caged-Ca^{2+} compounds/capacitance measurement/inositol trisphosphate/secretion

Introduction

The final Ca^{2+}-dependent steps of exocytosis in various types of cells recently have been shown to exhibit Ca^{2+} affinities in the micromolar range (Neher and Zucker, 1993; Thomas *et al.*, 1993; Heidelberger *et al.*, 1994; Muallem *et al.*, 1995; Kasai *et al.*, 1996). An extreme case is exocytosis involving synaptic vesicles in which the K_d for Ca^{2+} is expected to be 194 μM (Heidelberger *et al.*, 1994). The synaptic vesicles are co-localized with voltage-gated Ca^{2+} channels in the plasma membrane, and the rate constants for Ca^{2+} binding to putative Ca^{2+} sensors are large. Therefore, large increases in cytosolic Ca^{2+} concentration ($[Ca^{2+}]_i$) at the inner mouth of a Ca^{2+} channel can be detected by the Ca^{2+} sensors before calcium ions bind to Ca^{2+} binding molecules in the cytosol. The high $[Ca^{2+}]_i$ area formed by a Ca^{2+} channel is called a 'Ca^{2+} domain' (Chad and Eckert, 1984; Smith and Augustine, 1989), which is too small to be visualized by light microscopic Ca^{2+} imaging techniques.

Exocytosis is also triggered by Ca^{2+} release from intracellular Ca^{2+} stores which often induces a complex spatio-temporal pattern of $[Ca^{2+}]_i$ increases. The exocrine acinar cell is an excellent system for investigating the quantitative relationship between Ca^{2+} release and exocytosis, because most agonist-induced $[Ca^{2+}]_i$ increases are mediated by Ca^{2+} release from intracellular Ca^{2+} stores (Petersen *et al.*, 1994), and they occurred in a fixed spatial pattern (Kasai *et al.*, 1993). It has been reported that exocytotic secretion of enzyme from exocrine acinar cells requires micromolar $[Ca^{2+}]_i$ (Knight and Koh, 1984; Cher *et al.*, 1992; Stecher *et al.*, 1992; Muallem *et al.*, 1995; Padfield and Panesar, 1995). However, no Ca^{2+} imaging study has revealed large increases in $[Ca^{2+}]_i$ that can account for exocytosis of zymogen granules in acinar cells (Kasai and Augustine, 1990; Tan *et al.*, 1992; Toescu *et al.*, 1992; Kasai *et al.*, 1993; Maruyama *et al.*, 1993; Thorn *et al.*, 1993; Gerasimenko *et al.*, 1996). There are two possible reasons for the discrepancy. First, the zymogen granules might utilize Ca^{2+} in the Ca^{2+} domains at the inner mouth of Ca^{2+} release channels as synaptic vesicles do for voltage-gated Ca^{2+} channels. Second, there may be an area of a large $[Ca^{2+}]_i$ increase in acinar cells that was not detected in the previous studies because high affinity Ca^{2+} indicators, such as fura-2, that could be saturated with Ca^{2+} at a high $[Ca^{2+}]_i$, were used.

We therefore performed a Ca^{2+} imaging study using a low affinity Ca^{2+} indicator dye, benzothiazole coumarin (BTC) (Iatridou *et al.*, 1994) and a sensitive cooled-CCD camera that allowed us to capture images with a higher resolution (12 bits) (Messler *et al.*, 1996) than in previous studies (8 bits) (Kasai and Augustine, 1990; Toescu *et al.*, 1992). Ca^{2+} imaging with BTC revealed that agonists increased $[Ca^{2+}]_i$ to levels >10 μM at the apical pole of the secretory granule area, called a 'trigger zone' (Kasai *et al.*, 1993). The occurrence of these micromolar Ca^{2+} spikes appears to have a critical functional consequence: exocytosis in acinar cells requires $[Ca^{2+}]_i$ increases to levels >5 μM during the agonist-induced Ca^{2+} spikes as well as homogeneous $[Ca^{2+}]_i$ increases that were produced by photolysis of a caged-Ca^{2+} compound, nitrophenyl-EGTA (Ellis-Davies and Kaplan, 1994). Interestingly, lower concentrations of agonists induce submicromolar Ca^{2+} spikes which selectively activate Ca^{2+}-dependent ion channels, but do not induce the exocytosis. Thus, the distinct cellular functions are regulated by increases in $[Ca^{2+}]_i$ that can be measured using a Ca^{2+} imaging technique and whose physiological dynamic range is larger (0.1–15 μM) than hitherto considered.

Results

Micromolar Ca^{2+} spikes in pancreatic acinar cells
We examined the distribution of $[Ca^{2+}]_i$ in mouse pancreatic acinar cells using the low affinity Ca^{2+} indicator
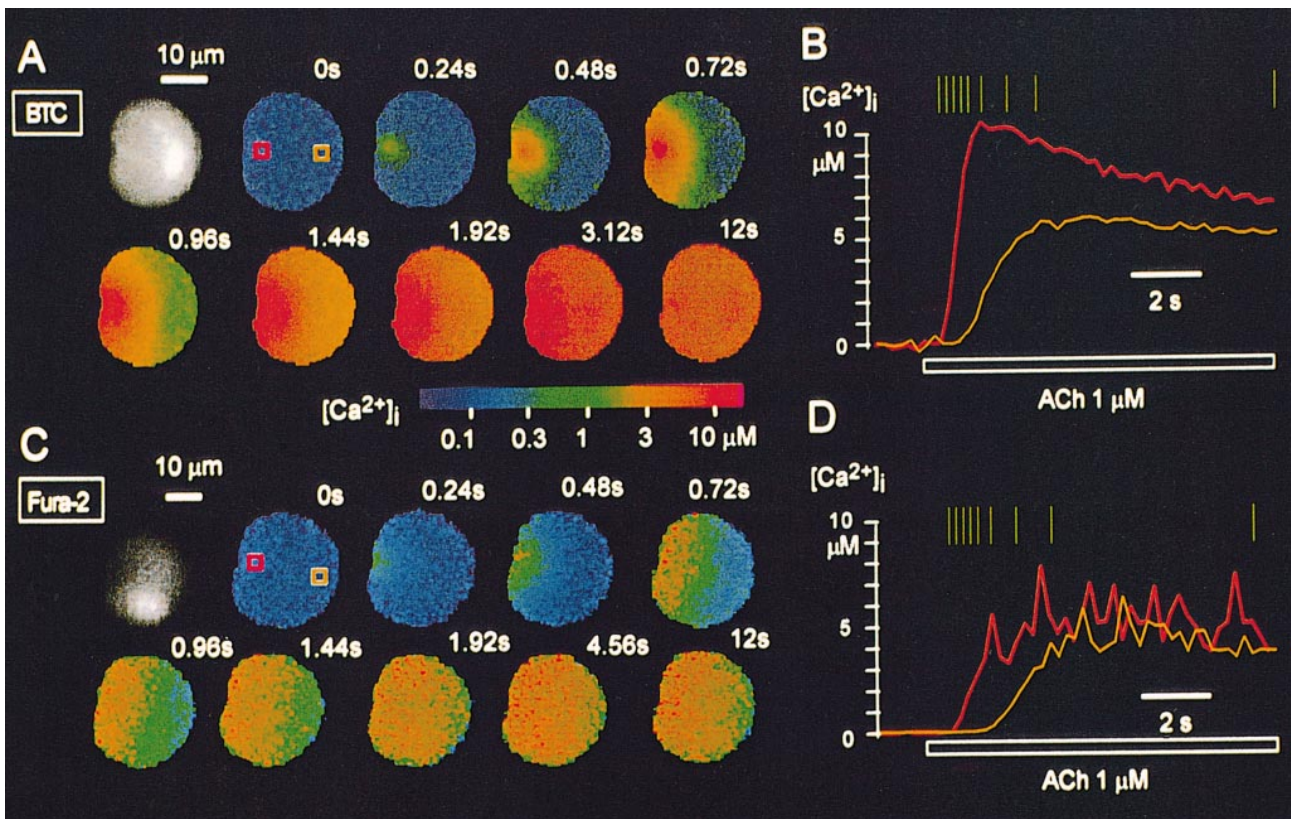
Fig. 1. Ca^{2+} imaging of mouse pancreatic acinar cells using BTC or fura-2. (**A**) and (**C**) Patterns of $[Ca^{2+}]_i$ increases induced by 1 μM ACh in two different cells. Black and white images are fluorescence images of acinar cells loaded with BTC (A) or fura-2 (C). The dark areas in the fluorescence images correspond to secretory granule areas. Colour images are Ca^{2+} images obtained at the time points indicated above the images and by vertical bars in (B) and (D). The Ca^{2+} images were constructed from R_{A2} (fura-2) and ΔR_{B4} (BTC) as described in Materials and methods. $[Ca^{2+}]_i$ is represented in terms of the pseudocolour scale shown in (A). (**B**) and (**D**) Average $[Ca^{2+}]_i$ within red and yellow squares in (A) (0 s) and (C) (0 s), respectively, plotted against time.

dye BTC ($K_{Ca}=10$ μM) (Iatridou *et al.*, 1994), which was loaded into the acinar cells via a patch pipette. A highly sensitive cooled-CCD camera with a 12 bit resolution (Messler *et al.*, 1996) was utilized to detect changes in fluorescence of BTC in a range of $[Ca^{2+}]_i$ between 0.3 and 100 μM (Materials and methods). Figure 1A shows the results of one such experiment. The dark areas in the fluorescence image correspond to secretory granule areas. Pseudocolour-coded BTC ratio images indicate that acetylcholine (ACh; 1 μM) induced an increase in $[Ca^{2+}]_i$ to 10 μM in the trigger zone and 5.5 μM in the basal area (Figure 1B). The peak $[Ca^{2+}]_i$ averaged over 14 cells was 9.89 ± 1.96 μM (mean $\pm$ SD) in the trigger zone and 5.4 ± 2.05 μM in the basal area. A large increase in $[Ca^{2+}]_i$ occurred in acinar cells upon their stimulation with cholecystokinin (CCK, 10 nM, $n = 5$) or with caged inositol trisphosphate (IP_3; 100 μM, $n = 5$, data not shown). A large increase in $[Ca^{2+}]_i$ also occurred in the cells in which the effects of whole-cell perfusion were minimized by means of a short 'whole-cell' episode (5 s) (Zhou and Neher, 1993) with a patch pipette containing 3 mM BTC, upon their stimulation with ACh (50 nM–1 μM, $n = 9$).

We noted two differences between the Ca^{2+} images obtained using BTC and those obtained using fura-2 (Figure 1C). First, the Ca^{2+} gradient, with the $[Ca^{2+}]_i$ peaking in the trigger zone, lasted >10 s in the BTC images, whereas the gradient was obscure or not present after the Ca^{2+} wave spread to the basal area in the fura-2 images (Figure 1C) (Kasai and Augustine, 1990; Toescu *et al.*, 1992). Second, the $[Ca^{2+}]_i$ started to dissipate at the trigger zone within a few seconds after its peak in the BTC images (Figure 1B), whereas it remained high in this zone in the fura-2 images (Figure 1C). These differences can be explained by the fact that the K_d of fura-2 for Ca^{2+} (0.2 μM) is 50 times smaller than that of BTC for Ca^{2+} (10 μM) and thus fura-2 can be saturated with Ca^{2+} at a high $[Ca^{2+}]_i$.

Two-indicator four-wavelength Ca^{2+} measurements

The differences in the spatio-temporal patterns of $[Ca^{2+}]_i$ measured with BTC and fura-2 might be due to cell to cell variation or to different effects of the two Ca^{2+} indicators on cytosolic buffering in acinar cells. To exclude these possibilities, the acinar cells were loaded simultaneously with fura-2 and BTC, and two ratios were acquired simultaneously for the same cell (see Materials and methods), taking advantage of the fact that the excitation wavelengths of fura-2 and BTC differ greatly (Grynkiewicz *et al.*, 1985; Iatridou *et al.*, 1994). Consistent with the results obtained using a single indicator, the standing luminal–basal Ca^{2+} gradient (Figure 2A, 0.68–3.08 s) and its quick dissipation (Figure 2A, 3.08–16.04 s; Figure 2B) were detected only in the BTC images, and not in the fura-2 images (Figure 2A and B). This indicates
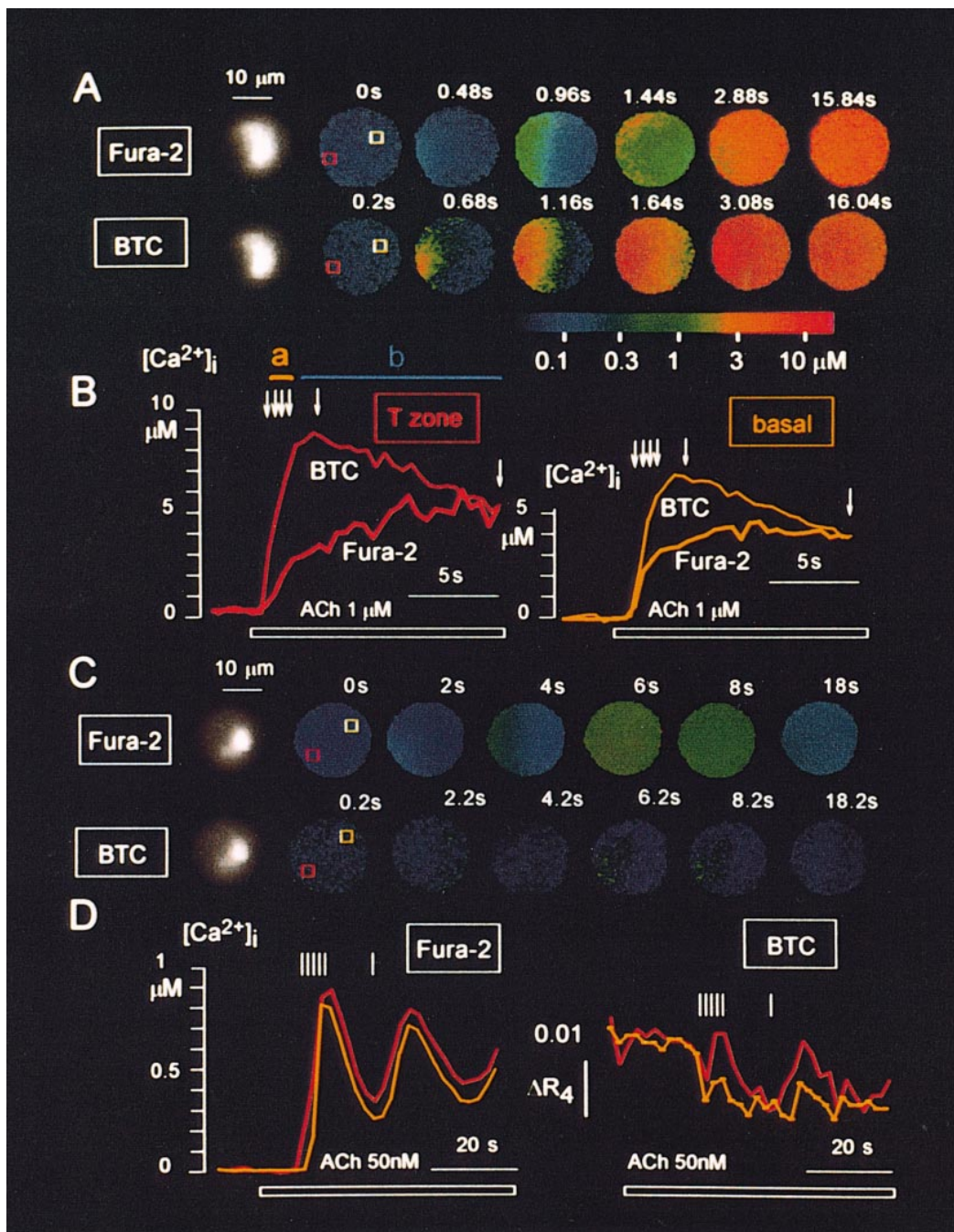
Fig. 2. Four-wavelength Ca^{2+} imaging using BTC and fura-2 simultaneously. (**A**) and (**C**) Ca^{2+} imaging of acinar cells loaded with 200 µM fura-2 and 350 µM BTC and stimulated with 1 µM ACh (A) and 50 nM ACh (C). Black and white images are fluorescence images of the acinar cells excited at 380 nm (fura-2) and 480 nm (BTC). Colour images are Ca^{2+} images obtained at time points indicated above the images and by arrows and vertical bars in (B) and (D), respectively. The Ca^{2+} images were constructed from R_2 (fura-2) and ΔR_4 (BTC). $[Ca^{2+}]_i$ is represented in terms of the pseudocolour scale shown in (A). (**B**) Average $[Ca^{2+}]_i$ within red (trigger zone or T zone) and yellow (basal area) squares shown in (A). Horizontal colour bars denoted by a or b indicate the periods in which differences between BTC and fura-2 images are observed (see text). (**D**) Average $[Ca^{2+}]_i$ (fura-2) and ΔR_4 (BTC) within red and yellow squares shown in (C).

that fura-2 was saturated during the Ca^{2+} spikes and confirms the occurrence of micromolar increases in $[Ca^{2+}]_i$.

Interestingly, the magnitude of the initial $[Ca^{2+}]_i$ increase at the trigger zone estimated using BTC (Figure 2A, 0.68 s) tended to be larger than that estimated using fura-2 [Figure 2A, 0.48 and 0.96 s, the period represented by the yellow bar (a) in Figure 2B] in all nine cells examined. This difference can be explained by saturation

of fura-2 within small areas of high $[Ca^{2+}]_i$ which cannot be resolved using the present imaging methods. The small areas might reflect hot spots in the trigger zone (Thorn *et al.*, 1996) and/or Ca^{2+} domains of Ca^{2+} release channels (Rizzuto *et al.*, 1993). In contrast, the $[Ca^{2+}]_i$ in the basal area estimated using fura-2 was similar to that estimated using BTC unless $[Ca^{2+}]_i$ increased to levels >2 µM which resulted in saturation of fura-2 (Figure 2A and B), indicating that the two indicators were calibrated correctly.
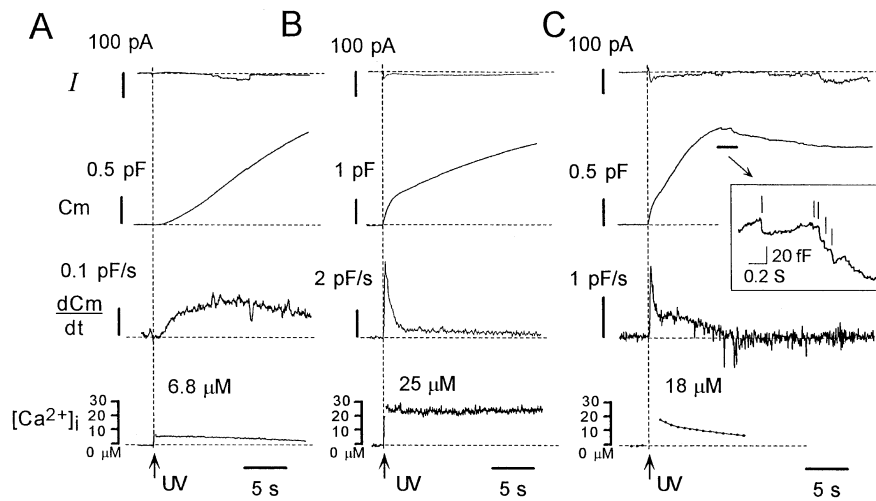
Fig. 3. Exocytosis in the acinar cells studied using NP-EGTA and capacitance measurement. (**A–C**) Capacitance measurements for three different acinar cells, where inorganic ions in both the pipette and external solutions were replaced with impermeant organic ions. The uppermost traces in (A–C) are current traces, indicating successful blockade of ion channels. The second and third traces show the membrane capacitance and its time derivatives, respectively. The lowermost traces show $[Ca^{2+}]_i$ estimated from ratiometric measurement using BTC. The peak $[Ca^{2+}]_i$ values are indicated. Pipettes contained 10 mM NP-EGTA, and were loaded with 1 mM $CaCl_2$ (A) or 5 mM $CaCl_2$ (B–C). The $[Ca^{2+}]_i$ was measured using a cooled-CCD camera in (C). The inset in (C) shows a magnified capacitance trace for the part denoted by the horizontal bar in the capacitance trace. Vertical bars indicate stepwise decreases in capacitance.

Details of the initial difference at the trigger zone will be reported in a separate paper. An apparent slow increase in $[Ca^{2+}]_i$ at the trigger zone as detected in fura-2 images [the period represented by the blue bar (b) in Figure 2B] occurred when the $[Ca^{2+}]_i$ estimated using BTC decreased. This is considered to have been due to cross-talk between fura-2 and BTC signals, as predicted, when $[Ca^{2+}]_i$ was higher than 2 μM (Materials and methods; Figure 7). A similar phenomenon was observed in the basal area (Figure 2B). In contrast, fura-2 images did not exhibit such a slow phase in one-indicator measurements (Figure 1C and D), supporting that the phenomenon was due to cross-talk.

Low concentrations of agonist could induce Ca^{2+} spikes whose amplitudes were <2 μM. In the example shown in Figure 2C, fura-2 images revealed submicromolar Ca^{2+} waves that originated in the trigger zone and spread throughout the basal area (Figure 2C). In contrast, BTC images revealed smaller $[Ca^{2+}]_i$ increases or even a slight reduction in $[Ca^{2+}]_i$ (Figure 2C and D). The slight reduction in $[Ca^{2+}]_i$ estimated using BTC must have been due to cross-talk between fura-2 and BTC signals, as was predicted (Materials and methods; Figure 7). This confirmed that increases in $[Ca^{2+}]_i$ never exceeded 2 μM. These patterns of Ca^{2+} spikes were detected in 7 out of 13 cells to which 0.1 μM ACh was applied. In addition, small Ca^{2+} spikes localized in the trigger zone were detected in 4 out of 11 cells to which 50 nM ACh was applied (data not shown) (Kasai *et al.*, 1993; Thorn *et al.*, 1993). Thus, we identified a total of three types of Ca^{2+} spikes.

Ca²⁺ dependence of exocytosis

We next examined Ca^{2+} and time dependences of exocytosis in the acinar cells by capacitance measurement and use of a method involving photolysis of the caged Ca^{2+} compound nitrophenyl EGTA (NP-EGTA). We blocked most of the Ca^{2+}-activated currents in these experiments to reduce the conductance changes (see

Materials and methods). The acinar cells exhibited a slow increase in membrane capacitance upon sudden increases in $[Ca^{2+}]_i$ (Ca^{2+} jumps) to between 5 and 8 μM (Figure 3A). There was an initial lag in the sigmoidally increasing capacitance (Figure 3A). The mean value of the delay was 2.3 ± 1.0 s (mean ± SD, $n = 23$). Larger Ca^{2+} jumps induced a faster capacitance increase in addition to the slow one (Figure 3B and C). The slow increase lasted as long as the $[Ca^{2+}]_i$ remained high (Figure 3B), while the capacitance sometimes decreased if the $[Ca^{2+}]_i$ decreased (Figure 3C). In such cases, we often detected stepwise decreases in capacitance (Figure 3C, inset), which were also detected in endocrine cells (Rosenboom and Lindau, 1994; Thomas *et al.*, 1994), and probably represented the formation of vacuoles (Baker and Knight, 1981; Knoll *et al.*, 1992; Back *et al.*, 1993). These features of exocytosis and endocytosis were qualitatively very similar to those reported in the case of endocrine cells (Thomas *et al.*, 1994; Kasai *et al.*, 1996), supporting the view that the changes in capacitance reflect exocytosis and endocytosis of secretory vesicles in the acinar cells.

The Ca^{2+} dependence of fast and slow increases in capacitance was determined by applying Ca^{2+} jumps of various magnitudes in acinar cells (Figure 4A). The slow component of exocytosis was detected at $[Ca^{2+}]_i$ as low as 5 μM, while the fast component of exocytosis appeared at $[Ca^{2+}]_i$ of 8 μM and became larger at higher $[Ca^{2+}]_i$. Rates of capacitance increases were quantified and are plotted in Figure 4B and C. The Ca^{2+} dependence of the slow exocytosis was fitted with a Hill equation with a dissociation constant of 8 μM and a Hill coefficient of 3 (solid curve). On the other hand, the Ca^{2+} dissociation constant and Hill coefficient of the fast exocytosis were 15 μM and 4, respectively. The Ca^{2+} dependence of the slow exocytosis is similar to results obtained by measuring amylase secretion from permeabilized acinar cells (Muallem *et al.*, 1995), suggesting that the slow exocytosis represents secretion of zymogen granules.
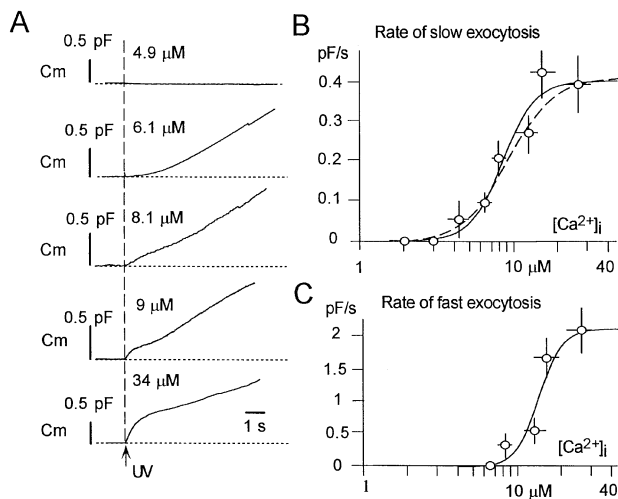
Fig. 4. Ca^{2+} and time dependence of exocytosis in acinar cells. (**A**) Capacitance traces for five different cells, where $[Ca^{2+}]_i$ was increased as indicated using NP-EGTA. (**B**) Ca^{2+} dependence of the rate of the slow exocytosis calculated from the slope of the steepest part of the slow exocytosis. (**C**) Ca^{2+} dependence of the rate of fast exocytosis calculated from the peak values of the time derivatives of capacitance traces. Each point in (B) and (C) is the average of 6–15 measurements. Vertical bars represent SE and horizontal bars SD. Solid curves in (B) and (C) are the best fits of the data using a Hill equation. Half-saturation is achieved at 8 and 15 μM for slow and fast exocytosis, respectively. Hill coefficients are 3 and 4 for slow and fast exocytosis, respectively. The dashed curve in (B) was drawn according to Equation 1 in the text.

Micromolar Ca^{2+} spikes and exocytosis

We then studied agonist-induced exocytosis using capacitance measurement and Ca^{2+} imaging. Ion channels were not blocked in these experiments (Figure 5) in order to allow examination of the activation of Ca^{2+}-dependent ion channels. A high concentration ($\geqslant 1$ μM) of ACh increased the $[Ca^{2+}]_i$ at the trigger zone to >5 μM, and induced increases in capacitance (Figure 5A). This conclusion was based on the results of 11 experiments in which Ca^{2+}-dependent currents and access resistance were <300 pA and 4 MΩ, respectively. Therefore, the capacitance changes should not be much affected by the conductance changes (Materials and methods). In fact, little change in capacitance was detected in acinar cells perfused with Ca^{2+} buffers (2 mM BAPTA and 0.8 mM $CaCl_2$) to reduce the peak $[Ca^{2+}]_i$ to <5 μM (Figure 5B), even though Ca^{2+}-dependent currents with larger amplitudes were recorded (Figure 5B). On the other hand, when the $[Ca^{2+}]_i$ did not reach 5 μM, little exocytosis was detected (Figure 5C) ($n = 7$ for 0.1 μM, $n = 6$ for 50 nM). This indicates that the agonist-induced exocytosis depends on $[Ca^{2+}]_i$, and that an increase in $[Ca^{2+}]_i$ to at least 5 μM is required, as was the case with the slow component of exocytosis induced by photolysis of NP-EGTA.

In contrast to the case for exocytosis, Ca^{2+}-dependent ionic currents were induced at $[Ca^{2+}]_i < 0.2$ μM. Figure 5C shows the data obtained during the imaging experiments shown in Figure 2C. Membrane potentials were clamped at the reversal potential of non-selective cation currents to allow selective recording of chloride currents (Kasai and Augustine, 1990). Chloride currents had two transient components as described previously (Kasai and Augustine, 1990). The first transient current appeared as soon as the
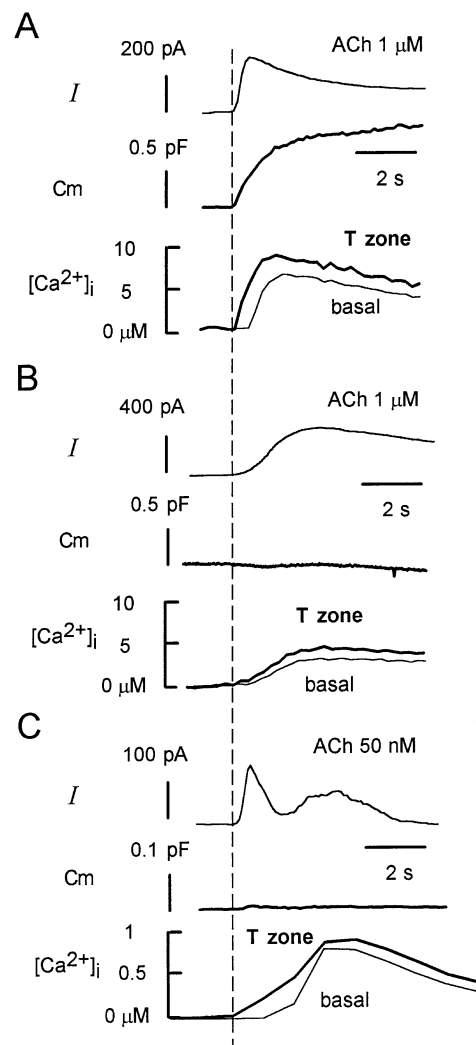

Fig. 5. ACh-induced Ca^{2+} gradients, exocytosis and chloride currents. (**A–C**) Current and capacitance measurements for three different acinar cells. The uppermost traces represent membrane current recorded at the reversal potential of Ca^{2+}-dependent cation current (0 mV), and the middle traces membrane capacitance. The lowermost traces show $[Ca^{2+}]_i$ at the trigger zone (T zone, thick line) and basal area (thin line). The acinar cells were stimulated with 1 μM (A and B) or 50 nM ACh (C). In order to reduce the peak $[Ca^{2+}]_i$, 2 mM BAPTA and 0.8 mM $CaCl_2$ were added to the pipette solution in (B). $[Ca^{2+}]_i$ was estimated using BTC (A and B) or fura-2 (C). The data shown in (C) were taken from the experiment shown in Figure 2C. A vertical dashed line indicates the onset of $[Ca^{2+}]_i$ increases at the trigger zone.

initial increase in $[Ca^{2+}]_i$ in the trigger zone was detected (Kasai and Augustine, 1990; Thorn *et al.*, 1993), indicating that the chloride current is induced at the area of the plasma membrane adjacent to the trigger zone. The current decayed even though the $[Ca^{2+}]_i$ at the trigger zone increased, suggesting that the decay was due to inactivation of chloride channels. When the Ca^{2+} waves reached the basal area, the second chloride current appeared, suggesting that the channels were distributed in the basolateral area (Kasai and Augustine, 1990). These results indicate that the ion channels and exocytosis were regulated differentially by Ca^{2+} spikes in a $[Ca^{2+}]_i$-dependent manner (Figure 6).
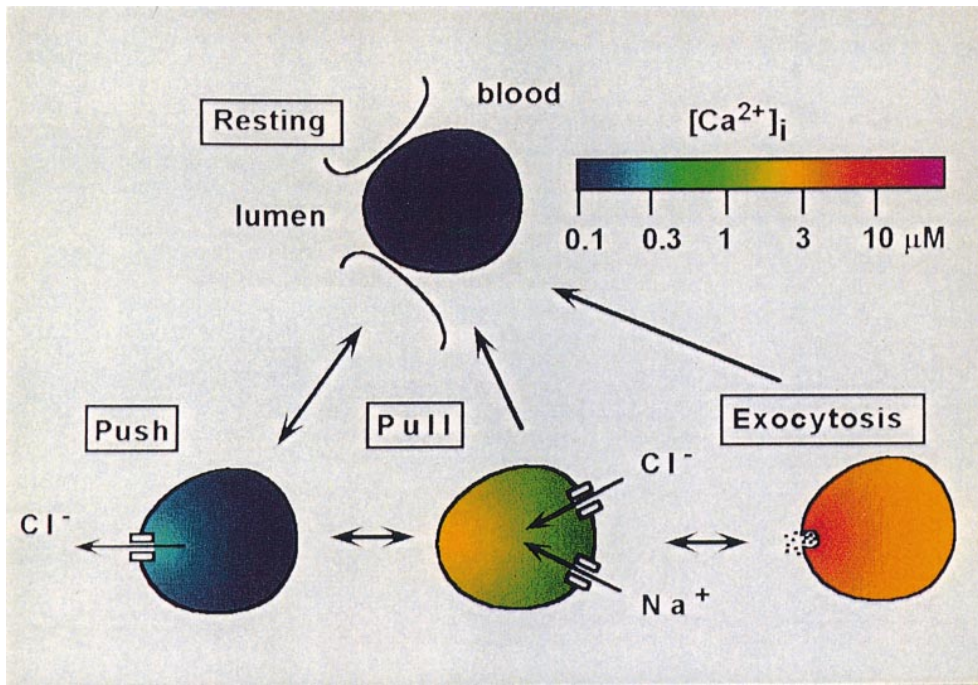
Fig. 6. Three active phases of the acinar cell. Local Ca²⁺ spikes at the trigger zone induce secretion of Cl⁻ into the lumen of an acinus (push phase). Global submicromolar Ca²⁺ spikes sequentially activate luminal and basal ion channels, and sequentially induce the push phase and uptake of Cl⁻ from blood (pull phase). A micromolar Ca²⁺ spike induces exocytosis of the zymogen granules (exocytosis phase). The occurrence of three active phases is regulated in an agonist concentration-dependent manner.

Discussion

Here, we have described the first investigation of Ca²⁺ signalling and exocytosis using a low affinity Ca²⁺ indicator, BTC, in pancreatic acinar cells. Our data demonstrate that agonists can evoke distinct Ca²⁺ spikes with widely differing amplitudes, i.e. micromolar and submicromolar ones. We will discuss below the characteristics and functional consequences of the multiple types of Ca²⁺ spikes in acinar cells.

Three types of Ca²⁺ spikes in acinar cells

Agonist-induced increases in [Ca²⁺]$_i$ to levels >10 µM were detected using a low affinity Ca²⁺-selective indicator, BTC, whose K_d for Ca²⁺ was estimated to be ~10 µM in both *in vitro* (Iatridou *et al.*, 1994) and *in vivo* calibration experiments (Materials and methods). Moreover, the two-indicator four-wavelength Ca²⁺ imaging results indicated that a high affinity Ca²⁺ indicator, fura-2, was saturated during the spikes (Figure 2A). Thus, in our imaging study, we consistently demonstrated that IP₃-dependent mechanisms are involved in the increase of [Ca²⁺]$_i$ to levels as high as 10 µM. Results of an earlier study suggested the occurrence of micromolar [Ca²⁺]$_i$ increases in the Ca²⁺ domains of Ca²⁺ release channels (Rizzuto *et al.*, 1993). Our findings further indicate that micromolar Ca²⁺ spikes that can be imaged directly using Ca²⁺ indicators occur in bulk cytosol.

The concentrations of Ca²⁺ measured using BTC routinely peaked at the trigger zone during the micromolar Ca²⁺ spikes (Figures 1 and 2). When we used a high affinity indicator, however, the [Ca²⁺]$_i$ peaked at the trigger zone only at the onset of the [Ca²⁺]$_i$ increases (Kasai *et al.*, 1993) (Figures 1C and 2A). This difference is explained by the saturation of the indicator at high
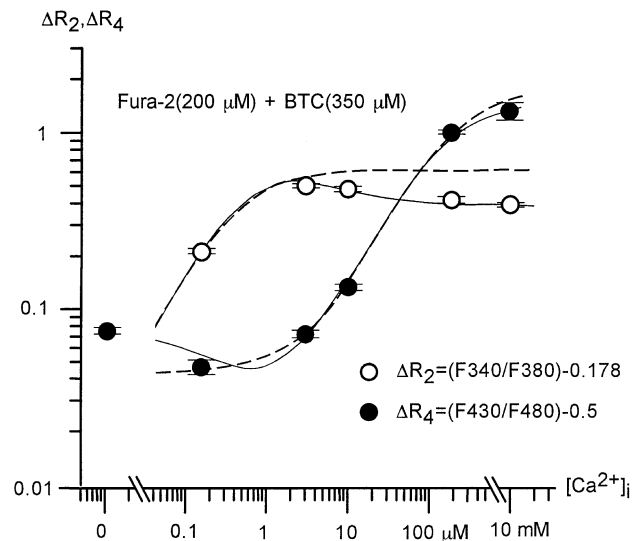

Fig. 7. Calibration curves for two-indicator four-wavelength Ca²⁺ measurement using fura-2 and BTC. The dependence of fluorescence ratios R_2 and R_4 on [Ca²⁺]$_i$ was predicted and measured directly in acinar cells using [Ca] calibration solutions. The abscissa represents [Ca²⁺]$_i$, and the ordinate $\Delta R_2 = R_2$–0.178 and $\Delta R_4 = R_4$–0.5 on a logarithmic scale, where 0.178 is the minimal value of R_2, and 0.5 is a value close to the minimal value of R_4 of 0.55. Solid curves are drawn according to Equation 5 in the text using the parameters measured *in vivo* in the presence of one of the Ca²⁺ indicators, assuming that the concentration of fura-2 was 200 µM and that of BTC was 350 µM. Filled and open circles represent mean values of ΔR_2 and ΔR_4, respectively, measured in acinar cells loaded with 200 µM fura-2 and 350 µM BTC. Vertical bars represent SEM. Dashed curves show fitting of the actual curve according to Equation 3.

[Ca²⁺]$_i$. Also, the highest estimates of [Ca²⁺]$_i$ in the basal area after the spread of Ca²⁺ waves to the basal area were obtained from fura-2 images in some studies (Kasai and

Augustine, 1990) but not in others (Kasai *et al.*, 1993; Thorn *et al.*, 1993). The results of imaging studies using fura-2 should be interpreted with caution, because fluorescence ratios of fura-2 are considerably affected by slight spatial heterogeneity in R_{max} of fura-2, because the estimated $[Ca^{2+}]_i$, $K_{Ca}\beta\Delta R/(R_{max}-R)$, critically depends on R_{max} (Grynkiewicz *et al.*, 1985) at $[Ca^{2+}]_i$ higher than 2 µM, where R becomes close to R_{max}. In contrast, the $[Ca^{2+}]_i$ estimated using BTC is more reliable at high $[Ca^{2+}]_i$, because R is not close to the R_{max} of the indicator if $[Ca^{2+}]_i$ is lower than 20 µM.

We have thus demonstrated that the micromolar Ca^{2+} spikes are induced with physiological concentrations of ACh or CCK, and are always spatio-temporally organized in such a manner that the Ca^{2+} spikes which initiate and peak at the trigger zone are transient and never exceed 15 µM (Figure 1A). Since IP_3 receptors are ubiquitous in animal cells, similar micromolar Ca^{2+} gradients may occur in other cells. We therefore expect our findings to prompt investigation of Ca^{2+} homeostasis using low affinity Ca^{2+} indicators in efforts to understand the physiology and pathology of cells.
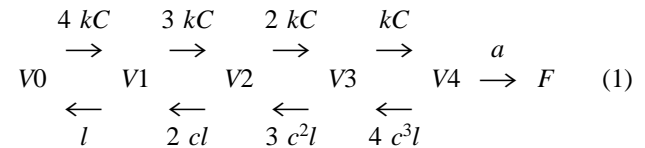
Importantly, low concentrations of agonists could trigger smaller Ca^{2+} spikes whose amplitudes do not greatly exceed 2 µM. This was confirmed by the results of the two-indicator four-wavelength imaging (Figure 2C). The submicromolar Ca^{2+} spikes originated at the trigger zone, and spread throughout the cell, as in the case of the micromolar Ca^{2+} spikes. Therefore, global Ca^{2+} spikes (Thorn *et al.*, 1993) can be either submicromolar or micromolar, depending on the agonist concentration. This is, to our knowledge, the first report of two types of Ca^{2+} waves having widely different amplitudes in the same cell. Since we also detected local Ca^{2+} spikes, restricted to the trigger zone, at low agonist concentrations (Kasai *et al.*, 1993; Thorn *et al.*, 1993), altogether three types of Ca^{2+} spikes have been identified by Ca^{2+} imaging in the acinar cells. The existence of multiple types of Ca^{2+} spikes is consistent with the incremental detection mechanisms of IP_3-induced Ca^{2+} release reported for acinar cells (Muallem *et al.*, 1989) and other preparations (Meyer and Stryer, 1990). The extent of spreading of Ca^{2+} waves and their amplitudes may be determined by a quantitative balance between the IP_3-dependent Ca^{2+} release and Ca^{2+} pumping (van de Put *et al.*, 1994). A precise molecular and theoretical understanding of the diversity in Ca^{2+} spikes and waves remains to be gained.

Ca²⁺ dependence of exocytosis and electrolyte secretion

Experiments involving both capacitance measurements and photolysis of a caged-Ca^{2+} compound revealed the occurrence of two components of exocytosis in exocrine acinar cells (Figures 3 and 4). We believe that slow exocytosis represents exocytosis of the zymogen granules, because its Ca^{2+} dependence correlates well with existing data on the secretion of amylase from permeabilized pancreatic acinar cells (Knight and Koh, 1984; Cher *et al.*, 1992; Stecher *et al.*, 1992; Muallem *et al.*, 1995; Padfield and Panesar, 1995). This is also consistent with results of a study on PC12 cells, in which the exocytosis of large dense core vesicles was slower and showed a higher affinity for Ca^{2+} than that of small clear vesicles (Kasai

et al., 1996; Ninomiya *et al.*, 1997). The fast exocytosis might represent exocytosis of other types of secretory vesicles, for example those carrying newly synthesized proteins (Arvan and Castle, 1987) or small clear vesicles which have not been identified in acinar cells.

In order to compare the kinetic features of the Ca^{2+}-dependent exocytosis of the zymogen granules in acinar cells and the synaptic vesicles in neurones, the release rates and delays were fitted with a model used to explain exocytosis of the synaptic vesicles (Heidelberger *et al.*, 1994):

$$V0 \underset{l}{\overset{4\,kC}{\underset{\rightarrow}{\leftarrow}}} V1 \underset{2\,cl}{\overset{3\,kC}{\underset{\rightarrow}{\leftarrow}}} V2 \underset{3\,c^2l}{\overset{2\,kC}{\underset{\rightarrow}{\leftarrow}}} V3 \underset{4\,c^3l}{\overset{kC}{\underset{\rightarrow}{\leftarrow}}} V4 \overset{a}{\rightarrow} F \quad (1)$$

where *V0–V4* represent vesicles whose Ca^{2+} binding sites are occupied by 0–4 Ca ions, F is a fused vesicle, k is the rate constant of Ca^{2+} binding, C the concentration of Ca^{2+}, l the rate constant of Ca^{2+} dissociation and a the rate constant of fusion. The parameter c accounts for the cooperativity of the Ca^{2+} binding (Heidelberger *et al.*, 1994), and is given the value 0.2 to account for the large Hill coefficient of the Ca^{2+} dependence (Figure 4B). a was <0.1/s, because the slow exocytosis lasted >10 s (Figure 3B), if the $[Ca^{2+}]_i$ increase was maintained. Therefore, the delay in exocytosis (2.3 s at $[Ca^{2+}]_i$ <10 µM) is attributed chiefly to a small k, and the Ca^{2+} dependence of the release rates (Figure 4) depends both on k and l. A satisfactory fit of these data can be obtained by setting k equal to 1×10^5/s/M and l equal to 6/s (dashed curve in Figure 4B).

These results indicate that the slow exocytosis in the acinar cells can be accounted for by a and k being >100 times smaller than those for the nerve terminal (Heidelberger *et al.*, 1994). The smaller a means that the $[Ca^{2+}]_i$ increases must persist for longer than a few seconds in order to induce secretion. The smaller k and a suggest that the exocytosis of zymogen granules is little affected by Ca^{2+} in the Ca^{2+} domain, but is regulated by Ca^{2+} in bulk cytosol. Consistent with this hypothesis, ACh triggered exocytosis only when a Ca^{2+} indicator detected $[Ca^{2+}]_i$ increases to levels >5 µM (Figure 5), and the agonist-induced micromolar Ca^{2+} spikes lasted more than a few seconds. It is possible that exocytosis takes place mostly at the area of the plasma membrane adjacent to the trigger zone, because the largest increases in $[Ca^{2+}]_i$ were detected there. It can then be speculated that disruption of the normal micromolar Ca^{2+} gradients triggers aberrant exocytosis, and results in acute pancreatitis (Ward *et al.*, 1995).

In contrast, during the submicromolar Ca^{2+} spikes, Ca^{2+}-dependent ion channels were activated without exocytosis (Figure 5C). In such a case, sequential activation of the Cl^-channels was detected, as reported previously, suggesting the existence of a push–pull mechanism of fluid secretion (Kasai and Augustine, 1990). Thus, the Ca^{2+} spikes can induce exocytosis and electrolyte secretion separately in a $[Ca^{2+}]_i$-dependent manner, as shown in Figure 6. According to this model, the three types of Ca^{2+} spikes trigger distinct cellular activities: the local Ca^{2+} spikes at the trigger zone cause secretion of Cl^- into the

lumen (push phase), the global submicromolar Ca^{2+} spikes induce uptake of Cl^- into the acinar cell (pull phase) and the micromolar Ca^{2+} spikes trigger exocytosis (exocytosis phase). During the push phase, Cl^- currents decayed, although the $[Ca^{2+}]_i$ was increasing at any part of the cell (Figure 2C). A similar decay in Ca^{2+}-dependent Cl^- currents was reported to occur in *Xenopus* oocytes (Parker and Yao, 1994). On the other hand, the Cl^- currents during the pull phase were sustained so long as the $[Ca^{2+}]_i$ remained high (Figure 5A–C). Our data suggest, therefore, that two types of Cl^- channels with distinctive distributions and regulation mechanisms are involved in electrolyte secretion from exocrine acinar cells.

In summary, our findings provide a new concrete example of Ca^{2+} release from intracellular stores regulating distinct cellular functions in an agonist concentration-dependent manner. In particular, we have found that exocytosis and electrolyte secretion are regulated by Ca^{2+} spikes with a wider dynamic range in their amplitudes than hitherto considered, i.e. micromolar and submicromolar Ca^{2+} spikes, respectively. These findings emphasize the value of using low affinity Ca^{2+} indicators in elucidating the functional roles of Ca^{2+} signalling in living cells.

Materials and methods

Recording solutions

Pancreatic acinar cells from 5- to 7-week-old mice were dissociated from pancreas by an enzymatic treatment as described (Maruyama, 1988). The dissociated cells were dispersed in a small chamber for electrophysiological recording in a recording solution (Sol A) containing 140 mM NaCl, 5 mM KCl, 2 mM $CaCl_2$, 1 mM $MgCl_2$, 10 mM Na–HEPES (Dojin, Kumamoto) and 10 mM glucose at pH 7.4 and 310 mOsm. ACh (Wako, Osaka) and CCK (Peptide Institute, Osaka) were dissolved in Sol A and applied to acinar cells via a glass pipette. Ca^{2+} indicators were dissolved in a solution (basic internal solution) containing 120 mM Cs glutamate, 5 mM CsCl, 50 mM Cs–HEPES, 1 mM ATP, 0.2 mM GTP and 2 mM $MgCl_2$ at pH 7.2, and indicator-containing solution was loaded into cells using the patch–clamp method. We used BTC and/or fura-2 (Molecular Probes, Eugene) as Ca^{2+} indicators. The concentrations of the indicators were 200 μM in single-indicator measurements, and 200 and 350 μM for fura-2 and BTC, respectively, in two-indicator measurements. Caged-IP₃ [D-*myo*-inositol 1,4,5-trisphosphate, P⁴⁽⁵⁾-1-(2-nitrophenyl)-ethyl ester, Calbiochem, San Diego] was added to the basic internal solution. As a caged-Ca^{2+} compound, we used 10 mM NP-EGTA (Molecular Probes) added with 5 mM $CaCl_2$. In order to reduce Ca^{2+}-induced ion currents during photolysis of NP-EGTA, we used an internal solution containing 105 mM N-methyl-D-glucamine (NMDG, Wako) glutamate, 50 mM NMDG–HEPES, 1 mM ATP and 0.2 mM GTP at pH 7.2. In addition, the solution surrounding a cell was perfused locally using a glass pipette ($\phi = 10$ μm) with an external solution containing 140 mM NMDG-glutamate, 10 mM NMDG–HEPES and 10 mM glucose at pH 7.4. Photolysis routinely induced increases in $[Ca^{2+}]_i$ to >10 μM. Smaller $[Ca^{2+}]_i$ increases were produced by loading NP-EGTA with lower concentrations of $CaCl_2$, i.e. 2.5, 2, 1 or 0.5 mM. If necessary, the pH of the solutions was readjusted using HCl. Osmolarities of the external and internal solutions were estimated to be ~310 mM after addition of all chemicals (Semi-Micro Osmometer, Knauer, Berlin, Germany). We carried out all methods under yellow light illumination (FL40S-Y-F, National, Tokyo, Japan) at room temperature, 22–25°C.

Ca²⁺ imaging setup

A recording chamber was placed on an inverted microscope (IMT-2, Olympus, Tokyo) and observed through an objective lens (DApo 40× UV/340 oil, Olympus). Measurement of $[Ca^{2+}]_i$ was performed using the Ca^{2+} indicators BTC and/or fura-2. Monochromatic beams of light with a wavelength of 340, 380, 430 or 480 nm were isolated from light emitted by a xenon lamp using a monochromator (T.I.L.L. Photonics, Munich), and fed into one port of a light guide (IMT-2-RFA caged, Olympus). The light was reflected by a dichroic mirror, DM500, placed

beneath the objective lens, and fluorescent light emitted from the cells was captured using a cooled-CCD camera system (T.I.L.L. Photonics) (Messler *et al.*, 1996) fixed at the side port of the IMT-2. During two-wavelength imaging, two images were captured successively at 430 and 480 nm for BTC, and at 340 and 380 nm for fura-2. The duration of image acquisition was 0.1 s, and the pairs of images were acquired every 0.24 s. During four-wavelength imaging, images were successively acquired for 0.1 s at 340, 380, 430 and 480 nm, and the same acquisition sequence was repeated every 0.48 or 2 s. Ratios of fluorescence intensities in two images were calculated after subtracting the background fluorescence. $[Ca^{2+}]_i$ was estimated from these ratios using the method described below, and represented by pseudocolour coding where 0.1, 0.3, 1, 3 and 10 μM were expressed as blue, sky blue, green, yellow and red, respectively (Figures 1 and 2).

One-indicator two-wavelength ratiometric Ca²⁺ imaging

Ratiometric estimation of $[Ca^{2+}]_i$ using either fura-2 or BTC was performed using the method developed by Grynkiewicz *et al.* (1985). Using their notation, fluorescence of an indicator (D), F_D, at four excitation wavelengths, λ_j (340, 380, 430 and 480 nm for j 0–3, respectively), is given by

$$F_{Dj} = Sf_{Dj} \, Cf_D + Sb_{Dj} \, Cb_D \tag{2}$$

where Sf_{Dj} and Sb_{Dj} represent the fluorescence of free and Ca^{2+}-bound indicators, respectively, and Cf_D and Cb_D represent the concentrations of free and Ca^{2+}-bound indicators, respectively. The fluorescence ratio $R_{Dj} = F_{D(j-2)}/F_{D(j-1)}$ for $j = 2$ or 4 is expressed as a monotonic function of Ca^{2+} concentration, [Ca], as,

$$R_{Dj} = \frac{R\min_{Dj} + R\max_{Dj} \dfrac{[Ca]}{K_D \beta_{Dj}}}{1 + \dfrac{[Ca]}{K_D \beta_{Dj}}} \tag{3}$$

where $R_{minDj} = Sf_{D(j-2)}/Sf_{D(j-1)}$, $R_{maxDj} = Sb_{D(j-2)}/Sb_{D(j-1)}$, $\beta_{Dj} = Sf_{D(j-1)}/Sb_{D(j-1)}$ and K_D represents the dissociation constant of the indicator for Ca^{2+}. Calibration experiments for fura-2 and BTC were carried out in acinar cells *in vivo* (Almers and Neher, 1985), and six constants were obtained: $R_{minA2} = 0.17$, $R_{maxA2} = 2.5$ and $K_A \beta_{A2} = 0.87$ for fura-2, and $R_{minB4} = 0.514$, $R_{maxB4} = 2.0$ and $K_B \beta_{B4} = 112$ for BTC ($n = 5$–12). Four [Ca] calibration solutions were prepared from the basic internal solution by adjusting its [Ca] to either 0 μM, 0.15 μM, 10 μM or 10 mM using Ca^{2+} buffers and $CaCl_2$. For the 0 μM and 10 mM [Ca] calibration solutions, we simply added 10 mM EGTA and 10 mM $CaCl_2$, respectively, to the internal solution. To prepare the 0.15 and 10 μM [Ca] calibration solutions, we used 1,2-bis(2-aminophenoxy)ethane-N,N,N′,N′-tetracetic acid (BAPTA, Molecular Probes) and 2-aminophenol-N,N,O-triacetic acid (APTRA, Molecular Probes), respectively, as Ca^{2+} buffers. We first added 20 mM BAPTA or 20 mM APTRA plus 8 mM $CaCl_2$ to the internal solution, and titrated [Ca] of the solution to 0.15 and 10 μM, respectively, with $CaCl_2$ using a mini Ca^{2+} electrode, which was made of polyethylene tubing ($\phi = 1.5$ mm), and a Ca^{2+} ionophore, ETH 129 (Fluka, Switzerland) (Baudet *et al.*, 1994). The [Ca] calibration solutions were whole-cell dialysed into the cells in the presence of a Ca^{2+} indicator, and fluorescence ratios were obtained after equilibration to give R_{minDj}, R_{maxDj} and $K_D \beta_j$. Our estimations were based on measurements in >5 cells.

Using Ca^{2+} images obtained using fura-2, distributions of R_{A2} were first calculated, and [Ca] was estimated as $K_A \beta_{A2}(R_{A2} - R_{minA2})/(R_{maxA2} - R_{A2})$ (Grynkiewicz *et al.*, 1985). Using Ca^{2+} images obtained using BTC, the distribution of R_{minB4} in individual cells was first estimated by averaging several frames of resting distribution of R_{B4}. This procedure was used to compensate for small heterogeneity in R_{minB4} (SD <0.01) within a cell, and to reduce noise levels particularly at $[Ca^{2+}]_i$ lower than 1 μM. Distributions of ΔR_{B4} were then calculated by subtracting the distribution of R_{minB4} from that of R_{B4}. Using ΔR_{B4}, [Ca] could be obtained as $K_{B4} \beta_{B4} \Delta R_{B4}/(R_{maxB4} - m[R_{minB4}] - \Delta R_{B4})$, where $m[R_{minB4}]$ represents the spatial average of R_{minB4}.

Two-indicator four-wavelength ratiometric Ca²⁺ imaging

As an extension of the above Equations 2 and 3 to the case in which two indicators are used simultaneously, the fluorescence of the indicators is given by

$$F_j = Sf_{Aj} \, Cf_A + Sb_{Aj} \, Cb_A + Sf_{Bj} \, Cf_B + Sb_{Bj} \, Cb_B \tag{4}$$

K.Ito, Y.Miyashita and H.Kasai

assuming a linear summation of the fluorescence of the two indicators. The ratio $R_j = F_{j-2}/F_{j-1}$ for $j = 2$ and 4 is expressed as

$$R_j = \frac{Rmin_{Aj} + Rmax_{Aj}\dfrac{[Ca]}{K_A\beta_{Aj}} + \dfrac{[B]\gamma_j}{[A]}\dfrac{1+[Ca]/}{K_A}\dfrac{}{1+[Ca]/}(Rmin_{Bj} + Rmax_{Bj}\dfrac{[Ca]}{K_B\beta_{Bj}})}{1 + \dfrac{[Ca]}{K_A\beta_{Aj}} + \dfrac{[B]\gamma_j}{[A]}\dfrac{1+[Ca]/K_A}{1+[Ca]/K_B}\ (1 + \dfrac{[Ca]}{K_B\beta_{Bj}})} \quad (5)$$

where $\gamma_j = Sf_{B(j-1)}/Sf_{A(j-1)}$, and [A] and [B] are concentrations of fura-2 and BTC, respectively. K_A and K_B were estimated as 0.2 and 10 μM, respectively, which are close to the values reported elsewhere (Grynkiewicz *et al.*, 1985; Iatridou *et al.*, 1994). Using whole-cell dialysis of [Ca] calibration solutions into the acinar cells and by calculating the ratios, we estimated $R_{minA4} = 15.3$, $R_{maxA4} = 2.7$, $K_A\beta_{A4} = 0.16$, $R_{minB2} = 0.18$, $R_{maxB2} = 0.124$ and $K_B\beta_{B2} = 3$ ($n = 5$–9). The *in vivo* values of γ_j were estimated as 0.263 and 131.6 for γ_2 and γ_4, respectively, in the presence of 200 μM fura-2, 350 μM BTC and 10 mM EGTA, according to the relationship $\gamma_j = [A](R_j-R_{minAj})/[B](R_{minBj}-R_j)$, which is derived from Equation 5. The small γ_2 and large γ_4 indicate that the amount of cross-talk between the two indicators is relatively small. On the basis of these values and Equation 5, the $[Ca^{2+}]_i$ dependences of R_2 and R_4 were predicted as smooth curves, shown in Figure 7. The predicted curves were confirmed by direct measurement of R_2 and R_4 in the presence of two indicators loaded into acinar cells at five different $[Ca^{2+}]_i$; 0, 0.15, 3, 10, 185 μM and 10 mM, as plotted in Figure 7 (circles). The 3 μM Ca^{2+}-buffered solution was prepared using 20 mM BAPTA, and its Ca^{2+} concentration was verified using the mini Ca^{2+} electrode.

The calibration curves can be approximated by the equation, $R_j = (R_{minj}+R_{maxj}[Ca]/K_j)/(1+[Ca]/K_j)$ for $j = 2$ and 4, where $R_{min2} = 0.185$, $R_{max2} = 0.85$, $K_2 = 0.3$, $R_{min4} = 0.545$, $R_{max4} = 2.35$ and $K_4 = 150$ μM (dashed curves in Figure 7). However, R_2 and R_4 are not monotonically increasing functions of [Ca] between 2 μM and 10 mM for R_2 and between 0 and 2 μM for R_4 where a decrease in R_2 and R_4 is detected (Figure 7, solid curves). The decreases are due to the small amount of cross-talk between the two indicators, and were also seen in actual experiments. R_4 decreased even when $[Ca^{2+}]_i$ increased, as shown in Figure 2D, and R_2 increased when $[Ca^{2+}]_i$ decreased (Figure 2A). Therefore, [Ca] could not be determined uniquely from R_2 and R_4 in the respective ranges of [Ca]. Outside the ranges mentioned above, however, R_2 and R_4 predicted [Ca] with <20% error (Figure 7, dashed and solid curves). Therefore, Ca^{2+} images were obtained from distributions of R_2 and ΔR_4 as was the case in the two-wavelength Ca^{2+} measurement, and [Ca] was estimated from $K_2(R_2-R_{min2})/(R_{max2}-R_2)$ and $K_4\Delta R_4/(R_{max4}-m[R_{min4}]-\Delta R_4)$, respectively, in these ranges. In order to facilitate comparison between R_2 and ΔR_4 images (Figure 2A), R_{max2} was adjusted slightly in each cell when necessary so that [Ca] during the recovery phase of agonist-induced Ca^{2+} transients was estimated similarly using both R_2 and ΔR_4. This correction only slightly affected (<10%) the estimate of [Ca] lower than 1 μM.

Photolysis of a caged-Ca^{2+} compound

Photolysis of a caged compound, NP-EGTA, was achieved as described (Kasai *et al.*, 1996; Ninomiya *et al.*, 1996). In brief, we used a mercury lamp (IMT-2-RFC, Olympus) as an actinic light source. The light from the mercury lamp was filtered through a 360 nm band-pass filter, and fed into one port of the light guide (IMT-2-RFA guide, Olympus). Incorporating a dichroic mirror, DM400, the light guide can accommodate two light sources, one for the actinic light and the other for excitation of a Ca^{2+} indicator. Irradiation with the actinic light was gated through an electric shutter (Copal, Tokyo). The duration of the opening of the shutter was set at 33 ms, which was sufficient for full activation of the caged compounds within the cells. The speed of the photolysis was not expected to affect the time course of exocytosis, which was slow in the case of the acinar cells.

In most studies in which a caged-Ca^{2+} compound was used, $[Ca^{2+}]_i$ was estimated by microfluorimetric measurement using a photomultiplier (NT5783, Hamamatsu Photonics, Hamamatsu, Japan) attached to the side port of an IMT-2 instead of the cooled-CCD camera. One ratiometric Ca^{2+} measurement and capacitance measurement were carried out simultaneously at 44 Hz. *In vivo* calibration experiments of BTC were

repeated in the presence of NP-EGTA (Zucker, 1992). We prepared a total of six calibration solutions that contained the basic internal solution plus 10 mM of either the caged or photolysed form of NP-EGTA. [Ca] of the calibration solutions was adjusted to either 0 μM, 20 μM or 10 mM with Ca^{2+} buffers and $CaCl_2$, and confirmed using the mini Ca^{2+} electrode as described above. R_{maxB4} and R_{minB4} were 2.45 and 0.55, respectively for both caged and uncaged NP-EGTA. Values of $K_B\beta_{B4}$ were 100 and 120 μM for caged and uncaged NP-EGTA, respectively. The values for photolysed caged-Ca^{2+} compounds were used to estimate the peak values of $[Ca^{2+}]_i$, since most of the caged-Ca^{2+} compounds were photolysed in our experiments (see below). Thus, $[Ca^{2+}]_i$ was estimated as $K_B\beta_{B4}\Delta R_{B4}/(R_{maxB4}-R_{B4})$. The error in the estimates of $[Ca^{2+}]_i$ during re-equilibration of caged Ca^{2+} compounds after photolysis was considered to be <16%.

Capacitance measurements

Capacitance measurements were carried out using a patch–clamp amplifier, AxoPatch 1D (Axon Instrument, Foster City) (Kasai *et al.*, 1996). When Ca^{2+} images were acquired, the time of image acquisition was monitored by recording the readout signal of the CCD camera during the capacitance measurement. The membrane potential of the cells was maintained at either 0 or –27 mV (these values were corrected for liquid junction potential), at which current–voltage relationships were almost linear and to which 1 kHz ($\omega = 6283$ radian/s) sine waves with a peak–peak amplitude of 50 mV were applied. Our experiments were performed using a total of 84 cells, where the initial membrane capacitance ranged between 8 and 14 pF (mean = 11.5, $n = 84$). Changes in capacitance were calculated from 10 cycles of sine waves and stored at 44 Hz. The phase-offset was corrected several seconds before application of Ca^{2+} jumps or agonists using the phase-tracking method (Fidler and Fernandez, 1989). For those experiments where ion currents were not blocked, ΔG of 10 nS (200 pA current at –20 mV) resulted in error of <23 fF [$C(\Delta G/Ga)^2$] (Maruyama *et al.*, 1993) when C was 10 pF, access resistance (Ga) was <5 MΩ and the phase offset was assumed to be corrected accurately. The inaccuracy in the correction of phase offset (θ) was estimated to be <0.05 radian using a capacitance calibration command generated by DC-1 option (Axon Instrument) [$\theta \doteq EG_{error}(\Delta C)/\omega EC_{error}(\Delta C)$] (Maruyama *et al.*, 1993). The inaccuracy in the correction of phase offset resulted in <83 fF error ($\theta\Delta G/\omega$) at ΔG of 10 nS (Maruyama *et al.*, 1993). Thus, overall error in the estimate of ΔC due to ΔG is <106 fF, which cannot account for the larger changes in ΔC actually detected (>500 fF, Figure 5A).

Acknowledgements

References

Almers,W. and Neher,E. (1985) The Ca signal from fura-2 loaded mast cells depends strongly on the method of dye-loading. *FEBS Lett.*, **192**, 13–18.

Arvan,P. and Castle,J.D. (1987) Phasic release of newly synthesized secretory proteins in the unstimulated rat exocrine pancreas. *J. Cell Biol.*, **104**, 243–252.

Back,N., Soinila,S. and Virtanen,I. (1993) Endocytotic pathways in the melanotroph of the rat pituitary. *Histochem. J.*, **23**, 133–139.

Baker,P. and Knight,D.E. (1981) Calcium control of exocytosis and endocytosis in bovine adrenal medullary cells. *Philos. Trans. R. Soc. Lond. Ser. B. Biol. Sci.*, **296**, 83–103.

Baudet,S., Hove-Madsen,L. and Bers,D.M. (1994) How to make and to use calcium-specific mini- and microelectrodes. In Nuccitelli,R. (ed.), *A Practical Guide to the Study of Calcium in Living Cells*. Academic Press, pp. 94–112.

Chad,J. and Eckert,R. (1984) Calcium 'domains' associated with individual channels may account for anomalous voltage relations of Ca-dependent responses. *Biophys. J.*, **45**, 993–999.

Cher,D.J., Padfield,P.J. and Jamieson,J.D. (1992) Amylase release from streptolysin O permeabilized fetal pancreatic acini. *Am. J. Physiol.*, **262**, G719–G726.

Ellis-Davies,G.C. and Kaplan,J.H. (1994) Nitrophenyl-EGTA, a photolabile chelator that selectively binds Ca^{2+} with high affinity and releases it rapidly upon photolysis. *Proc. Natl Acad. Sci. USA*, **91**, 187–191.

Fidler,N. and Fernandez,J.M. (1989) Phase tracking: an improved phase detection technique for cell membrane capacitance measurements. *Biophys. J.*, **56**, 1153–1162.

Gerasimenko,O.V., Gerasimenko,J.V., Belan,P.V. and Petersen,O.H. (1996) Inositol triphosphate and cyclic ADP-ribose-mediated release of Ca^{2+} from single isolated pancreatic zymogen granules. *Cell*, **84**, 473–480.

Grynkiewicz,G., Poenie,M. and Tsien,R.Y. (1985) A new generation of Ca^{2+} indicators with greatly improved fluorescence properties. *J. Biol. Chem.*, **260**, 3440–3450.

Heidelberger,R., Heinemann,C., Neher,E. and Matthews,G. (1994) Calcium dependence of the rate of exocytosis in a synaptic terminal. *Nature*, **371**, 513–515.

Iatridou,H., Foukaraki,E., Kuhn,M.A., Marcus,E.M., Haugland,R.P. and Katerinopoulos,H.E. (1994) The development of a new family of intracellular calcium probes. *Cell Calcium*, **15**, 190–198.

Kasai,H. and Augustine,G.J. (1990) Cytosolic Ca^{2+} gradients triggering unidirectional fluid secretion from exocrine pancreas. *Nature*, **348**, 735–738.

Kasai,H., Li,Y. and Miyashita,Y. (1993) Subcellular distribution of Ca^{2+} release channels underlying Ca^{2+} waves and oscillations in exocrine pancreas. *Cell*, **74**, 669–677.

Kasai,H., Takagi,H., Ninomiya,Y., Kishimoto,T., Ito,K., Yoshida,A., Yoshioka,T. and Miyashita,Y. (1996) Two components of exocytosis and endocytosis in PC12 cells studied using caged-Ca^{2+} compounds. *J. Physiol.*, **494**, 53–65.

Knight,D.E. and Koh,E. (1984) Ca^{2+} and cyclic nucleotide dependence of amylase release from isolated rat pancreatic acinar cells rendered permeabilized by intense electric fields. *Cell Calcium*, **5**, 401–418.

Knoll,G., Plattner,H. and Nordmann,J. (1992) Exo-endocytosis in isolated peptidergic nerve terminals occurs in the sub-second range. *Biosci. Rep.*, **12**, 495–501.

Maruyama,Y. (1988) Agonist-induced changes in cell membrane capacitance and conductance in dialysed pancreatic acinar cells of rats. *J. Physiol.*, **406**, 299–313.

Maruyama,Y., Inooka,G., Li,Y., Miyashita,Y. and Kasai,H. (1993) Agonist-induced localized Ca^{2+} spikes directly triggering exocytotic secretion in exocrine pancreas. *EMBO J.*, **12**, 3017–3022.

Messler,P., Harz,H. and Uhl,R. (1996) Instrumentation for multiwavelength excitation imaging. *J. Neurosci. Methods*, in press.

Meyer,T. and Stryer,L. (1990) Transient calcium release induced by successive increments of inositol 1,4,5-triphosphate. *Proc. Natl Acad. Sci. USA*, **87**, 3841–3845.

Muallem,S., Pandol,S.J. and Beeker,T.G. (1989) Hormone-evoked calcium release from intracellular stores is a quantal process. *J. Biol. Chem.*, **264**, 205–212.

Muallem,S., Kwiatkowska,K., Xu,X. and Yin,H.L. (1995) Actin filament disassembly is a sufficient final trigger for exocytosis in nonexcitable cells. *J. Cell Biol.*, **128**, 589–598.

Neher,E. and Zucker,R.S. (1993) Multiple calcium-dependent processes related to secretion in bovine chromaffin cells. *Neuron*, **10**, 21–30.

Ninomiya,Y., Kishimoto,T., Miyashita,Y. and Kasai,H. (1996) Ca^{2+}-dependent exocytotic pathways in CHO fibroblasts revealed by capacitance measurement and a caged-Ca^{2+} compound. *J. Biol. Chem.*, **271**, 17751–17754.

Ninomiya,Y., Kishimoto,T., Yamazawa,T., Ikeda,H., Miyashita,Y. and Kasai,H. (1997) Kinetics diversity in the fusion of exocytotic vesicles. *EMBO J.*, **16**, in press.

Padfield,P.J. and Panesar,N. (1995) Ca^{2+} dependent amylase secretion from SLO-permeabilized rat pancreatic acini requires diffusible cytosolic proteins. *Am. J. Physiol.*, **269**, G647–G652.

Parker,I. and Yao,Y. (1994) Relationship between intracellular Ca^{2+} signals and Ca^{2+}-activated Cl^- current in *Xenopus* oocytes. *Cell Calcium*, **15**, 276–288.

Petersen,O.H., Petersen,C.C.H. and Kasai,H. (1994) Calcium and hormone action. *Annu. Rev. Physiol.*, **56**, 297–319.

Rizzuto,R., Brini,M., Murgia,M. and Pozzan,T. (1993) Microdomains with high Ca^{2+} close to IP_3-sensitive channels that are sensed by neighboring mitochondria. *Science*, **262**, 744–747.

Rosenboom,H. and Lindau,M. (1994) Exo-endocytosis and closing of the fission pore during endocytosis in single pituitary nerve terminals internally perfused with high calcium concentrations. *Proc. Natl Acad. Sci. USA*, **91**, 5267–5271.

Smith,S. and Augustine,G.J. (1989) Calcium ions, active zones and synaptic transmitter release. *Trends Neurosci.*, **11**, 458–465.

Stecher,B., Ahnert-Hilger,G., Weller,U., Kemmer,T.P. and Gratzl,M. (1992) Amylase release from streptolysin O-permeabilized pancreatic acinar cells. *Biochem. J.*, **283**, 899–904.

Tan,Y.P., Marty,A. and Trautmann,A. (1992) High density of Ca^{2+}-dependent K^+ and Cl^- channels on the luminal membrane of lacrimal acinar cells. *Proc. Natl Acad. Sci. USA*, **89**, 11229–11233.

Thomas,P., Wong,J.G., Lee,A.K. and Almers,W. (1993) A low affinity Ca^{2+} receptor controls the final steps in peptide secretion from pituitary melanotrophs. *Neuron*, **11**, 93–104.

Thomas,P., Lee,A.K., Wong,J.G. and Almers,W. (1994) A triggered mechanism retrieves membrane in seconds after Ca^{2+}-stimulated exocytosis in single pituitary cells. *J. Cell Biol.*, **124**, 667–675.

Thorn,P., Lawrie,A.M., Smith,P.M., Gallacher,D.V. and Petersen,O.H. (1993) Local and global Ca^{2+} oscillations in exocrine cells evoked by agonists and inositol trisphosphate. *Cell*, **74**, 661–668.

Thorn,P., Moreton,R. and Berridge,M. (1996) Multiple, coordinate Ca^{2+}-release events underlie the inositol trisphophate-induced local Ca^{2+} spikes in mouse pancreatic acinar cells. *EMBO J.*, **15**, 999–1003.

Toescu,E.C., Lawrie,A.M., Petersen,O.H. and Gallacher,D.V. (1992) Spatial and temporal distribution of agonist-evoked cytoplasmic Ca^{2+} signals in exocrine cells analysed by digital image microscopy. *EMBO J.*, **11**, 1623–1629.

van de Put,F.M.M., De Pont,J.J.H.H.M. and Willems,P.H.G.M. (1994) Heterogeneity between intracellular Ca^{2+} stores as the underlying principle of quantal Ca^{2+} release by inositol 1,4,5-trisphophate in permeabilized pancreatic acinar cells. *J. Biol. Chem.*, **269**, 12438–12443.

Ward,J.B., Petersen,O.H., Jenkins,S.A. and Sutton,R. (1995) Is an elevated concentration of acinar cytosolic free ionised calcium the trigger for acute pancreatitis? *Lancet*, **346**, 1016–1019.

Zhou,Z. and Neher,E. (1993) Mobile and immobile calcium buffers in bovine adrenal chromaffin cells. *J. Physiol.*, **469**, 245–273.

Zucker,R.S. (1992) Effects of photolabile calcium chelators in fluorescent calcium indicators. *Cell Calcium*, **13**, 29–40.